

## CHAPTER 2

### *Experimental Details*

*The detailed experimental procedures and various characterization techniques employed in these studies are documented in this chapter. Three different types of conductive particles were used as filler viz. carbon black (CB), aluminum (Al), copper (Cu). Polymethylmethacrylate (PMMA) and polyvinylchloride (PVC) were used as polymer matrix for making composites. The brief descriptions of facility used for exposing the composites materials are described.*

## 2.0 Introduction

This chapter deals with the description of the materials (polymer and filler) used in the present work. The brief descriptions of facility used for exposing the composites materials to ion beam are described. The various characterization techniques used in the present study have been discussed in detail.

### 2.1 Materials used

#### 2.1.1 Poly (methyl methacrylate) (PMMA)

PMMA is well-known transparent polymer perspex; it is one of the lightest polymers known. PMMA is made by polymerizing the methyl methacrylate monomer. It is typically used for

**Optics:** Sun glasses, watch glasses, lenses, magnifying glasses

**Vehicles:** Rear lights, indicators, tachometer covers, warning triangles

**Electrical engineering:** Lamp covers, switch parts, dials, control buttons

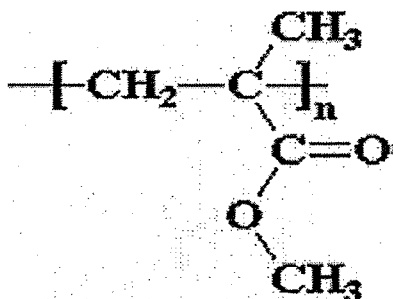
**Office equipment:** Writing and drawing instruments, pens

**Medicine:** Packaging for tablets, pills, capsules, suppositories, urine containers, sterilisable equipment.

**Others:** Leaflet dispensers, shatter-resistant glazing, shower cubicles, transparent pipelines, illuminated signs, toys.

#### *(1) General physical properties*

Molecular formula:  $\{C_5O_2H_8\}_n$



Density: 1.19 g/cm<sup>3</sup>

Glass transition temperature ( $T_g$ ): 110 °C

Melting Temperature ( $T_m$ ): 140 °C

Refractive index range: 1.49-1.51

### **Electrical properties**

PMMA has good insulating properties, a high dielectric strength and high tracking resistance. The relatively high surface resistance, however, encourages electrostatic charges on the surface of moulded parts; this can be largely overcome by the use of antistatic agents.

### **Optical properties**

PMMA is naturally transparent and colourless. The transmission for visible light is 92%. The refractive index is 1.492.

### **Natural colour**

PMMA is crystal clear and has a high surface gloss. It can be produced in all colours, transparent and muted.

### ***(ii) Synthesis of PMMA films***

Polymethylmethacrylate (PMMA) (molecular weight 36000) was purchased from Vesbo Company Turkey. The preparation of polymer films was carried out by solution cast technique with tetrahydrofuran (THF) as a solvent. The appropriate amount of high molecular weight PMMA was dissolved in THF solution and stirred for 4 hours to achieve a homogeneous, viscous solution. The solution thus obtained was cast on a glass plate and allowed to evaporate slowly inside a desiccator.

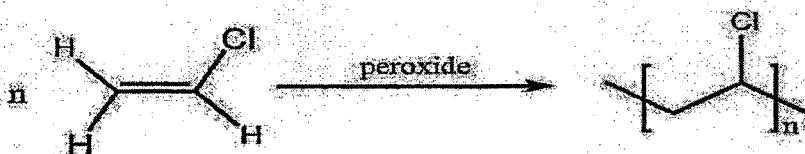
### **2.1.2 Poly (vinyl chloride) (PVC)**

Polyvinylchloride (PVC), widely known as vinyl, is one of the largest volume synthetic

thermoplastic used globally. Polyvinylchloride is a very unique polymer compared to

other widely used thermoplastics, due to its superior fire performance. Due to the excellent performance in combustion of polyvinylchloride, it's widely used in wide variety of applications including electric cables, upholstery, mattresses, wall linings, and floor coverings etc.

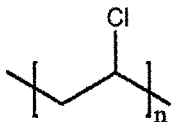
It is synthesized by free radical polymerization of vinyl chloride in presence of peroxide. It acquires softness by the addition of plasticizers.



#### ***(i) General Physical Properties***

Chemical formula:  $\{\text{CH}_2-\text{CH}(\text{Cl})\}_n$

Structure of PVC:



Density:  $1.3 \text{ g/cm}^3$

Glass transition temperature ( $T_g$ ):  $87^\circ\text{C}$

Melting temperature ( $T_m$ ):  $212^\circ\text{C}$

#### ***(ii) Synthesis of PVC films***

Poly vinyl chloride (PVC) (molecular weight 15000) was purchased from Vesbo Company Turkey. The preparation of polymer films was carried out by solution cast technique with tetrahydrofuran (THF) as solvent. The appropriate amount of high molecular weight PVC was dissolved in THF solution and stirred for 4 hours to achieve a homogeneous, viscous solution. The solution thus obtained was cast on a glass plate and allowed to evaporate slowly inside a dessicator.

### 2.1.3 Polypropylene (PP)

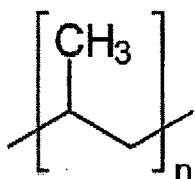
The good mechanical characteristics and the low cost make it a first material choice for many applications and PP has grown in some cases by displacing other polymers. PP has a very low surface energy and this makes it difficult to bond, join or coat due to the difficulty of 'wetting' the surface. PP is a crystalline polymer and the crystal formation after processing can lead to significant dimensional changes for some time after ejection from the mould.

Polypropylene is a largely non-polar, partially crystalline thermoplastic with a crystallinity of 60 to 70%. PP has a density of 0.90 to 0.91 g/cm<sup>3</sup> which is amongst the lowest densities for all plastics. PP does not absorb moisture.

The glass transition temperature of PP homopolymers is about 0°C. The material is viscous above this temperature. The creep strength of PP falls very sharply at high temperatures. The strength in one direction can be increased many times over by stretching. This is due to orientation of the macromolecules under a tensile stress.

#### *(i) General physical properties*

Structure:



Density: 0.90 to 0.91 g/cm<sup>3</sup>

Glass transition temperature (T<sub>g</sub>): 0°C

Melting Temperature (T<sub>m</sub>): 175°C

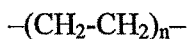
### 2.1.4 High density polyethylene (HDPE)

HDPE is a rigid, translucent solid. HDPE has a low degree of branching and thus stronger intermolecular forces and tensile strength. HDPE can be produced by

chromium/silica catalysts, Ziegler-Natta catalysts or metallocene catalysts. HDPE is used in products and packaging such as electrical insulation , milk jugs, detergent bottles, margarine tubs, garbage containers and water pipes.

***(i) General physical properties***

Chemical formula



Density: 0.941 g/cm<sup>3</sup>

Glass transition temperature (T<sub>g</sub>) :-110<sup>0</sup>C

Melting temperature (T<sub>m</sub>): 110<sup>0</sup>C

**2.1.5 Fillers**

The important filler materials used in making conductive composites are metal particles and graphite and carbon black material.

***(i) Graphitic and carbon-based materials***

The carbon-based fillers are produced by controlled pyrolysis of carbonaceous materials, primarily hydrocarbon fuels in the case of carbon blacks and organic polymer fibers in the case of graphite fibers. The fiber materials are available in a variety of product forms, including continuous filament, chopped fiber, and nonwoven mats of varying weights. Examples of this class of fillers include carbon black, graphite fibers, nickel-coated graphite fibers, etc.

***(i.a) Carbon black***

Commercially available high structure of carbon black with particle size ranging from 30-40 μm was purchased from Alfa Aesar (USA)

Properties of CB powder:

**Appearance:** Black powder

**Atomic Weight:** 12.0107

**Melting Point:** 3823 K (3550°C or 6422°F)

**Boiling Point:** 4098 K (3825°C or 6917°F)

**Density:** 2.2670 grams per cubic centimeter

**Phase at Room Temperature:** Solid

**Element Classification:** Non-metal

**(ii) Metal Particles.**

The most electrically and thermally conductive class of fillers consists of metal particles. Metals of primary importance are aluminum, copper, nickel, iron, stainless steel and silver. Silver is the most expensive and also the most conductive. Iron, copper and aluminum are relatively inexpensive, but all oxidize readily. The oxide layer on the particle surface can reduce effective conductivity significantly. Nickel and stainless steel, while resistant to heavy oxidation, are expensive compared to copper, iron or aluminum. Stainless steel is also considerably less conductive than the pure metals. Low loadings of metal particles are desirable because the metals are denser than the polymer matrix resins, thus increasing the weight of composite parts. Also, most metal fillers provide no structural reinforcement.

**(ii.a) Aluminum powder (Al)**

Al is known to be self passivation metal. The self passivated amorphous oxide layer ( $Al_2O_3$ ) forms an insulating boundary layer outside the metallic core (Al). Al metal powder with average particle size of the order of 63  $\mu m$  was purchased from Alfa Aesar (USA).

Properties of Aluminum

Appearance: Gray

**Atomic Number:** 13

**Atomic Weight:** 26.9815386

**Melting Point:** 933.437 K (660.323°C or 1220.581°F)

**Boiling Point:** 2792 K (2519°C or 4566°F)

**Density:** 2.70 grams per cubic centimeter

**Phase at Room Temperature:** Solid

**Element Classification:** Metal

*(ii.b) Copper (Cu) metal powder*

Cu metal powder with average particle size of the order of 50  $\mu\text{m}$  was purchased from Alfa Aesar (USA).

**Appearance:** Brown

**Atomic Number:** 29

**Atomic Weight:** 63.546

**Melting Point:** 1357.77 K (1084.62°C or 1984.32°F)

**Boiling Point:** 2835 K (2562°C or 4644°F)

**Density:** 8.933 grams per cubic centimeter

**Phase at Room Temperature:** Solid

**Element Classification:** Metal

In the present work, we have selected carbon black (CB), Aluminum (Al), and copper (Cu) metals.

## **2.2 Target Preparation**

### **2.2.1 Preparation of PMMA composites**

#### **Synthesis of Carbon black, Aluminum powder and copper metal dispersed PMMA composites**

Polymethylmethacrylate (PMMA) of molecular weight 36000 and different conductive additives like carbon black, Al, and Cu with particle size of the order of

35, 63 and 50  $\mu\text{m}$  respectively were used for the preparation of composites. The filler concentration was varied from 10- 40% (w/w) in the composites. Filled PMMA composites were prepared by mixing of carbon black(CB), aluminum(Al) and copper (Cu) fillers with polymer (PMMA) matrix by means of solution casting method. Tetrahydrofuran (THF) was used as a solvent to dissolve the polymer. The mixture of polymer and fillers was stirred at ambient temperature using magnetic stirrer at a high speed of around 700 rpm until all polymer grains were dissolved. After obtaining a homogeneous mixture, the mixture was poured on clean glass trough. The solvent was evaporated at ambient temperature ( $25^{\circ}\text{C}$ ,  $1^{\circ}\text{C}$ ) to get films (thickness of samples are given in Table 2.1) of polymer composites which were then dried in vacuum oven at  $30^{\circ}\text{C}$  [1].

### **2.2.2 Preparation of PVC composites**

#### **Synthesis of Carbon black, Aluminum powder and copper metal dispersed PVC composites**

Polyvinylchloride (PVC) of molecular weight 15000 different conductive additives like carbon black, metal powder (Al, Cu) with particle size of the order of 35, 63 and 50  $\mu\text{m}$  respectively were used for the preparation of composites.. The filler concentration was varied from 10- 40% (w/w) in the composites. Filled PVC composites were prepared by mixing carbon black(CB), aluminum(Al) and copper (Cu) fillers with PVC matrix by means of solution casting method. Tetrahydrofuran (THF) was used as a solvent to dissolve the polymer. The mixture of polymer and fillers was stirred at ambient temperature using magnetic stirrer at a high speed of around 700 rpm until all polymer grains were dissolved. After obtaining a homogeneous mixture, the mixture was poured on clean glass trough. The solvent was evaporated at ambient temperature ( $25^{\circ}\text{C}$ ,  $1^{\circ}\text{C}$ ) to get films (thickness of samples are

given in Table 2.1) of polymer composites which were then dried in vacuum oven at 30°C [1].

### 2.2.3 PP/TiO<sub>2</sub> composite

Polypropylene/TiO<sub>2</sub> composite of master batch in composition of 35% PP and 65% TiO<sub>2</sub> pellet of thickness 3.0 mm and of diameter 12.0 mm were supplied by Dizayn group of Company, Turkey.

### 2.2.4 PP/GF composite

The pellets of polypropylene glass fibers composites ( diameter 12.0 mm and thickness 2.0 mm) of master batch in compositions of 98% PP and 2% GF was supplied by Vesbo Company, Turkey.

### 2.2.5 HDPE/CB composite

The pellets of high density polyethylene carbon black composites ( diameter 12.0 mm and thickness 2.0 mm) of master batch in compositions of 98% HDPE and 2% CB was supplied by Vesbo Company, Turkey.

### 2.2.6 Thickness measurement of the composite films

The thickness of chemically synthesized composites was measured by a sensitive digital instrument. Sensitivity of the instrument was 0.001 mm. The thickness of the polymers was measured at 4-5 places chosen randomly and average of it was taken.

The obtained thicknesses are listed in Table 2.1.

**Table 2.1 Thickness of pure polymer and polymer composites**

Sample	Thickness (in $\mu\text{m}$ )
Pure PMMA	120
PMMA+CB	130
PMMA+Al	120
PMMA+Cu	120
Pure PVC	100
PVC+CB	150
PVC+Al	130

PVC+Cu	110
--------	-----

Thickness of commercially available pallet samples

Sample	Thickness (in mm)
PP+TiO <sub>2</sub>	3.0
PP+GF	2.0
HDPE+CB	2.0

### 2.3 Irradiation Facility at IUAC, New Delhi

Pelletron is a type of electrostatic particle accelerator similar to a Van de Graaff generator. Pelletrons have been built in many sizes, from small units producing voltages up to 500 kilovolts (kV) and beam energies up to mega electron volt (MeV) of kinetic energy, to the largest system, which has reached a DC voltage of over 25 megavolts and produced ion beams with energies over 900 MeV. Generating electric charge is done by a mechanical transportation system made of a chain of pellets (short conductive tubes connected by links made of insulating material), that is used to build-up high voltages on the Pelletron terminal. The system is enclosed by a pressure vessel filled with insulating gas, such as SF<sub>6</sub> (sulfur hexafluoride), and an evacuated beamline. The potential difference between the terminal and ground is used to accelerate several kinds of particles, such as positrons, electrons and negative and positive ions.

In the present work, a 15 UD Pelletron Accelerator located at IUAC New Delhi provided high energy heavy ion beam [2-5]. It is basically a tandem electrostatic accelerator of Van de Graff type, in vertical configuration, which can go upto a

maximum terminal voltage of 16 MV and capable of accelerating any ion from proton to uranium upto an energy of around 200 MeV or so depending upon the suitable negative ion source and the charge state. The schematic view of IUAC Pelletron and its different parts are given in figure 2.1.

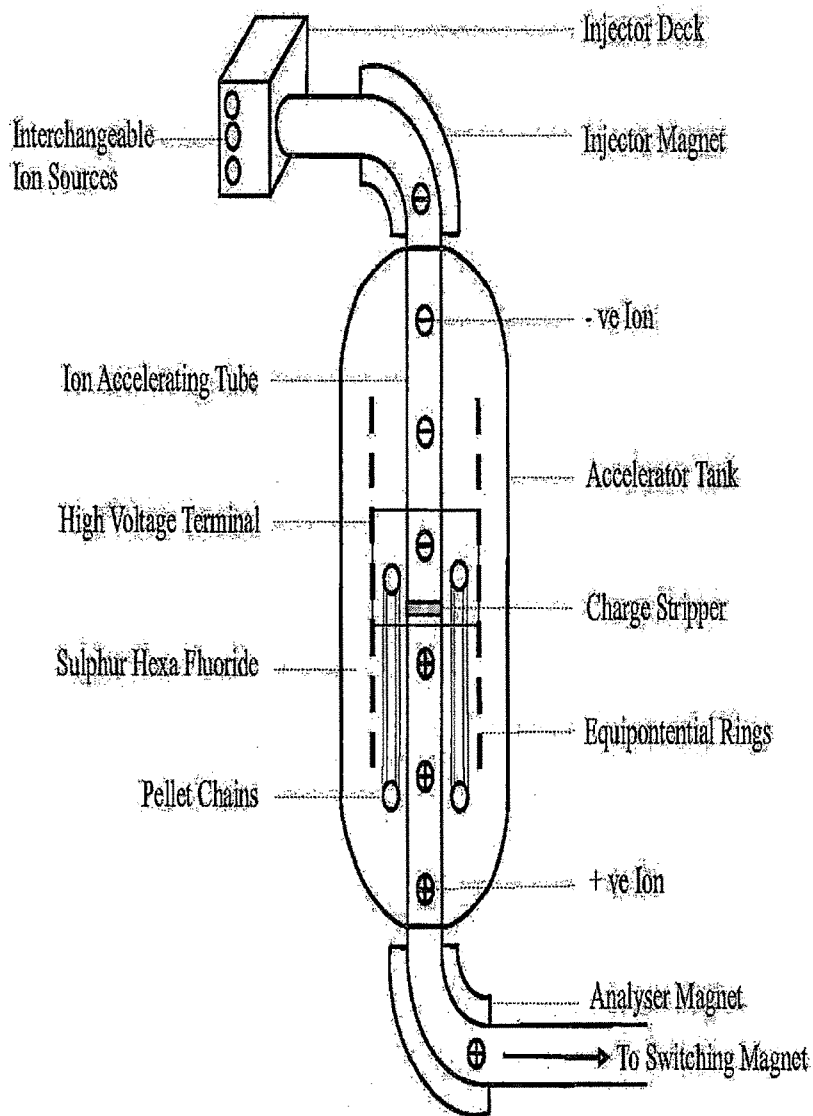


**Fig. 2.1 A schematic diagram showing the principle of acceleration of ions in Pelletron**

### 2.3.1 Theory



The pelletron accelerator consists mainly of two parts- ion source and the accelerating column with many auxiliary parts in between. In the top portion of the tank there are three different ion sources, namely R.F. source (ALPHATROSS), Source of Negative Ions by Cesium Sputtering (SNICS) and direct extraction negative ion source (Duoplasmatron), which can produce different negative ions to be injected in pelletron tank. These three ion sources work on three different principles and with the help of these; one can produce almost every type of negative ions. Duoplasmatron works on the principle of gas discharge, SNICS uses surface ionization and R.F. source utilizes high frequency gas discharge. The negative ions emerging from the ion source are first accelerated to 250 keV by the high voltage deck potential. The injector magnet does mass selection by bending the ions by  $90^\circ$  and then injects them into the accelerating tube. The singly ionized negative ions then follow a vertical downward path and get accelerated through the accelerating tube path. It consists of a vertical insulating cylindrical tank of height 26.5 m and diameter 5.5 m, filled with SF<sub>6</sub> (Sulphur hexa-fluoride) at the high pressure of ( $> 200$  psi) as an insulating gas. In the top portion of the tank there is an ion source system consisting of a high negative potential deck, SNICS, vacuum system, power supplies and controls of the ion source required to produce and inject the negative ions into accelerating tank. The mass selection of ions is done by the injector magnet. The ion source system is followed by the high voltage accelerating terminal of height 3.18 m and diameter 1.52 m inside the tank. The terminal is connected to the tank vertically through ceramic titanium tubes called accelerating tubes. A potential gradient is maintained through these tubes from high voltage to ground, from top of the tank to the terminal as well as from the terminal to the bottom of the tank. The insulating column which supports the high potential terminal consists of 31 MV modules, 15 on either side of the terminal. The

upper portion of the column is referred to as low energy section and the portion below the terminal as the high energy section. The shorted section with no potential gradient, commonly known as the Dead Section, is provided each, in the low and high energy sections for equipment housing. Both are provided with an electron trap and a sputter ion pump. The low energy dead section (LEDS) is also provided with an electrostatic quadrupole lens while the high energy dead section (HEDS) is equipped with a second foil stripper assembly. A shorting rod system is also provided for temporarily shorting selected column modules without entering the pressure vessel. Two insulating shafts run one from each ground end to the terminal and are used to drive four 400 cycle per second (cps) generators, which provide power for the equipments like heater lenses, pumps, foil changer etc., housed in the column , dead sections and terminal. The charging of high voltage terminal to 15 MV is done by using the pelletron charging chains. There are two independent sub systems with one charging chain in each, so that each chain is required to supply 100  $\mu$ A current. Negative ions from the ion source are focused by different optical instruments and then injected by the injector magnet into accelerator with some small energy ( $\gg$  300 keV) provided by the negative potential deck at the ion source. In the terminal, negative ions are stripped for few electrons by the positive ions which are again accelerated as they proceed towards the bottom of the tank at the ground potential. The beam energy gained by the ion in the accelerating tube at the end of the tube is determined by,

$$E_{beam} = (q + 1)V_T$$

where  $V_T$  is the terminal voltage,  $q$  is the number of positive charges on the ion after stripping. These high energy ions were analyzed to the required energy with the help of 90° bending magnet known as analyzer magnet and directed to the desired experimental area with the help of switching magnet which can deflect the beam into

any one of the seven beam lines in the beam hall for the experiments [6, 7]. Figure 2.2 shows that the Materials science chamber for ion beam irradiation.



**Fig. 2.2 Material science chamber for irradiation at IUAC New Delhi.**

### **2.3.2 Calculation of range and energy loss by SRIM Code**

SRIM is a computer code developed by J.F. Ziegler [8] for calculating the stopping power and penetration range of ions (10 eV - 2 GeV/amu) in matter using a full quantum mechanical treatment of ion-atom collisions (this refers to the moving atom as an "ion", and all target atoms as "atoms"). This calculation is made very efficient by the use of statistical algorithms which allow the ions to make jumps between calculated collisions and then averaging the collision results over the intervening gap. During the collisions, the ion and atom have a screened Coulombic collision,

including exchange and correlation interaction between the overlapping electron shells. The ion has long range interactions creating electron excitation and plasmons within the target. These are described by collective electronic structure and interatomic bond structures of target, when calculation is setup, the table of nominal values are supplied. The charge state of the ion within the target is described using the concept of effective charge, which includes a velocity dependent charge state and long range screening due to the collective electron sea of the target.

Thus SRIM code can be used to calculate the ion distribution and for quick calculation of damage, detailed calculation with full damage cascades, calculation of surface sputtering, Electron/ Neutron/Photon cascades, various ion energy/angle/positions, special multilayers biological targets, stopping power for ions in gases and the stopping of ions in compounds.

### **Results obtained from SRIM**

In the present work we have calculated the projected range, nuclear stopping power and electronic stopping power of 140 MeV Ag<sup>11+</sup> ions in PMMA, PVC, PP and HDPE using code SRIM 2003[9].

The projected range, electronic energy loss ( $S_e$ ) and nuclear energy loss ( $S_n$ ) of 140 MeV Ag<sup>11+</sup> ions in PMMA was found to be 24  $\mu\text{m}$ ,  $9.6 \times 10^2 \text{ eV/A}^0$  and  $2.9 \text{ eV/A}^0$  respectively.

The projected range, electronic energy loss ( $S_e$ ) and nuclear energy loss ( $S_n$ ) of 140 MeV Ag<sup>11+</sup> ions in PVC was found to be 21  $\mu\text{m}$ ,  $1.09 \times 10^3 \text{ eV/A}^0$  and  $3.59 \text{ eV/A}^0$  respectively.

The projected range, electronic energy loss ( $S_e$ ) and nuclear energy loss ( $S_n$ ) of 140 MeV Ag<sup>11+</sup> ions in PP was found to be  $\sim 27 \mu\text{m}$ ,  $8.495 \times 10^2 \text{ eV/A}^0$ ,  $2.503 \text{ eV/A}^0$  respectively.

The projected range, electronic energy loss( $S_e$ ) and nuclear energy loss ( $S_n$ ) of 140 MeV  $Ag^{11+}$  ions in HDPE was found to be  $\sim 26 \mu m$ ,  $8.778 \times 10^2 eV/A^0$ ,  $2.587 eV/A^0$  respectively.

In all the cases, maximum energy of the ion beam was lost by electronic interactions. The thickness of the polymer is larger than the projected range of ion beam in the polymer. Hence the beam was stopped in the polymer and maximum dissipation of heat took place at the end. The composite shows a lower projected range due to increase in density after doping fillers.

### 2.3.3 Irradiation and fluence estimations

The films were exposed to 140 MeV  $Ag^{11}$  ions in the materials science facility of the 15 UD pelletron at Inter University Accelerator Centre, New Delhi. The irradiation of the films was carried out ambient temperature under vacuum of the order of  $10^{-6}$  Torr for time periods ranging from 120 to 1200 seconds. Table 2.2 shows the irradiation details of different samples.

The total numbers of ions falling on the target were estimated to be in the range of  $1 \times 10^{11}$  ions/cm<sup>2</sup> to  $5 \times 10^{12}$  ions/cm<sup>2</sup> depending on the ion current and the time of bombardment. The ion beam was defocused using magnetic scanning system, so that an area of  $1 \times 1$  cm<sup>2</sup> was uniformly irradiated. The beam current was kept low and was monitored intermittently with a Faraday cup. Fig.2.3 shows the polymer composites samples after ion beam irradiation mounted on the target ladder. It can be seen that the color of the films(samples) changes due to ion beam irradiation.

The ion fluence was estimated by time of irradiation and beam current as follow,

$$I = \frac{Q}{T} = \frac{Dqe}{T}$$

$$I = \frac{\phi Aqe}{T}$$

$$T = \frac{\phi A q e}{I}$$

Where, I = ion current (nA)

Q= total charge

D= dose = ion fluence ( $\phi$ ) in ions/cm<sup>2</sup> x area (A) of irradiation in cm<sup>-2</sup>

q= charge state

e= electronic charge =  $1.6 \times 10^{-19}$  C

T= Time of irradiation (Sec)

Since, the number of particles per nano ampere of beam current

$$= \frac{I}{q e} (pnA)$$

$$T = \frac{\phi A}{\text{beam current (pnA)}}$$

Using above equation, the required time was calculated for each fluence. During experiment, keeping current of the ion beam constant, the sample was irradiated for the pre-determined time for a particular fluence.

**Table 2.2 Irradiation details of the samples**

S.No	Sample Name	Fluences(ions/cm <sup>2</sup> )	Current (pNA)	Energy & Ion
1	Pure PMMA	$1 \times 10^{11}$ , $1 \times 10^{12}$	0.5	140MeV, Ag <sup>11+</sup>
	PMMA+10%CB	$1 \times 10^{11}$ , $1 \times 10^{12}$	0.5	
	PMMA+20%CB	$1 \times 10^{11}$ , $1 \times 10^{12}$	0.5	
	PMMA+30%CB	$1 \times 10^{11}$ , $1 \times 10^{12}$	0.5	
	PMMA+40%CB	$1 \times 10^{11}$ , $1 \times 10^{12}$	0.5	
2	PMMA+10%Al	$1 \times 10^{11}$ , $1 \times 10^{12}$	0.5	140MeV, Ag <sup>11+</sup>
	PMMA+20%Al	$1 \times 10^{11}$ , $1 \times 10^{12}$	0.5	

	PMMA+30%Al	$1 \times 10^{11}$ , $1 \times 10^{12}$	0.5	
	PMMA+40%Al	$1 \times 10^{11}$ , $1 \times 10^{12}$	0.5	
3	PMMA+10%Cu	$1 \times 10^{11}$ , $1 \times 10^{12}$	0.5	140MeV, Ag <sup>11+</sup>
	PMMA+20%Cu	$1 \times 10^{11}$ , $1 \times 10^{12}$	0.5	
	PMMA+30%Cu	$1 \times 10^{11}$ , $1 \times 10^{12}$	0.5	
	PMMA+40%Cu	$1 \times 10^{11}$ , $1 \times 10^{12}$	0.5	
4	Pure PVC	$1 \times 10^{11}$ , $1 \times 10^{12}$	0.5	140MeV, Ag <sup>11+</sup>
	PVC+10%CB	$1 \times 10^{11}$ , $1 \times 10^{12}$	0.5	
	PVC+20%CB	$1 \times 10^{11}$ , $1 \times 10^{12}$	0.5	
	PVC+30%CB	$1 \times 10^{11}$ , $1 \times 10^{12}$	0.5	
	PVC+40%CB	$1 \times 10^{11}$ , $1 \times 10^{12}$	0.5	
5	PVC+10%Al	$1 \times 10^{11}$ , $1 \times 10^{12}$	0.5	140MeV, Ag <sup>11+</sup>
	PVC+20%Al	$1 \times 10^{11}$ , $1 \times 10^{12}$	0.5	
	PVC+30%Al	$1 \times 10^{11}$ , $1 \times 10^{12}$	0.5	
	PVC+40%Al	$1 \times 10^{11}$ , $1 \times 10^{12}$	0.5	
6	PVC+10%Cu	$1 \times 10^{11}$ , $1 \times 10^{12}$	0.5	140MeV, Ag <sup>11+</sup>
	PVC+20%Cu	$1 \times 10^{11}$ , $1 \times 10^{12}$	0.5	
	PVC+30%Cu	$1 \times 10^{11}$ , $1 \times 10^{12}$	0.5	
	PVC+40%Cu	$1 \times 10^{11}$ , $1 \times 10^{12}$	0.5	
7	PP/TiO <sub>2</sub>	$1 \times 10^{11}$ , $5 \times 10^{12}$	0.5	140MeV, Ag <sup>11+</sup>
8	PP/GF	$1 \times 10^{11}$ , $5 \times 10^{12}$	0.5	140MeV, Ag <sup>11+</sup>
9	HDPE/CB	$1 \times 10^{11}$ , $5 \times 10^{12}$	0.5	140MeV, Ag <sup>11+</sup>

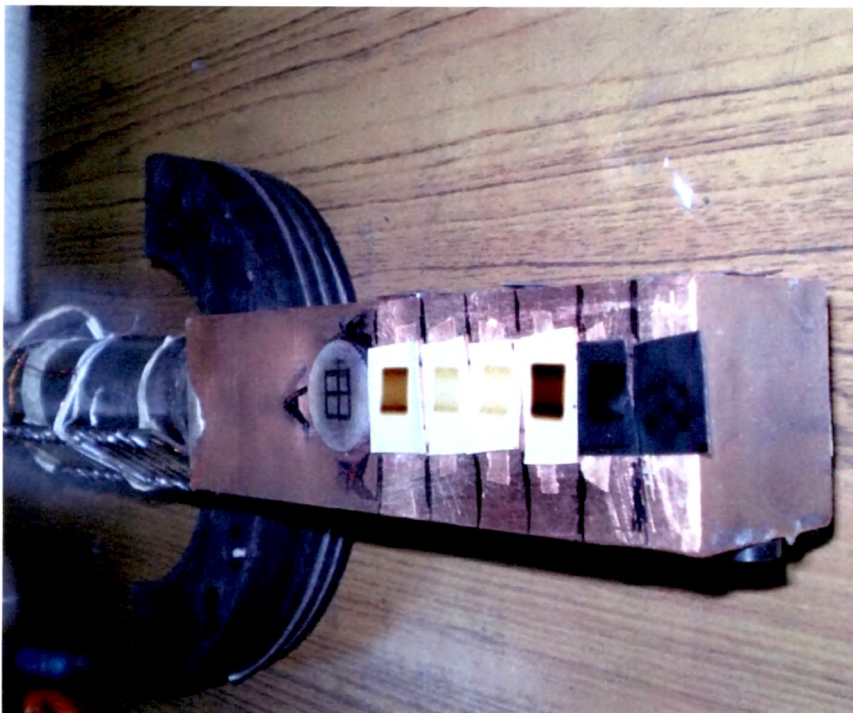


**Fig. 2.3 Polymer composites samples after irradiation.**

## **2.4 Characterization Techniques**

The pristine and irradiated samples were analysed with different characterization techniques to study their physical, chemical, structural, thermal properties and surface morphology. Different characterization techniques with their working principle and specifications are discussed in the following subsections.

### **2.4.1 Dielectric Spectroscopy**

Dielectric spectroscopy depends on the polarization, which is induced in the material due to the effect of an external electrical stress. Dielectric spectroscopy is used because it is a good tool to probe the internal structure of systems by means of observing macroscopic parameters, which are easily measurable. It is also non-invasive making it suitable for materials, which change characteristics when subjected to any form of stress. Dielectric materials were initially investigated by J.C Maxwell [10]. This work was continued by Debye at the beginning of the last century (Debye 1912). Debye's theory is based on dielectric losses, which is concerned with

polarization and relaxation of electric dipoles [11]. His model is based on non-interacting dipoles floating freely in a viscous medium and assumes that the rate of polarisation relaxation is directly proportional to polarization, i.e.  $dP/dt \propto P$ . Experiments, which the model was based on, were performed on dilute solutions. Later investigations showed that this theory is not applicable to solid materials. In 1981, Dissado and Hill have also developed a theory of dielectric response [12-18]. According to Dissado and Hill theory at high frequency, intra-cluster motions are dominant. In intra-cluster motions, the relaxation of dipole will produce a 'chain' response in its neighboring dipoles and the reaction of neighboring dipole will, in turn affect the first dipole, so the overall effect will be seen as single cluster dipole moment relaxation. This reduces the dielectric constant at these frequencies.

This thesis presents the dielectric characteristics of the Polymer metal composite materials in the frequency domain (100Hz to 10 MHz) as well as temperature from room temperature to 80°C. Measurements were made on the samples before and after ion beam irradiation.

**(i) Theory**

In order to describe the dielectric properties of the material considered a thin parallel plate capacitor held in a vacuum. If the capacitor is charged the potential established across the capacitor would be

$$V_0 = Q_0/C_0 \dots\dots\dots(2.4.1)$$

$Q_0$  ,  $C_0$  are the charge and capacitance of the capacitor in vacuum.

The ratio of the voltages defines the permittivity of the dielectric,  $\epsilon$ ,

$$\epsilon = \frac{V_0}{V} = \frac{C}{C_0} \dots\dots\dots(2.4.2)$$

C is the capacitance of the capacitor with the dielectric inserted. The voltage across the capacitor can be written as

$$V = \frac{Q_0}{\epsilon C_0} = \frac{Q}{C_0} \dots\dots\dots(2.4.3)$$

$Q_0$  is known as the true charge,  $Q$  is known as the free charge since it is the portion of true charge which contributes to the voltage. The difference between the true and free charges is the bound charge ( $Q_0 - Q$ ). The charge is bound by an adjacent charge of an equal magnitude and opposite sign, which lies in the surface of the dielectric.

Polarization,  $P$ , is defined as the surface density of the bound charge.

Polarization is the difference in charge density contributed by the material, see Figure 2.4. To understand the source of polarization induced in the material by the electric field, polarization unit can be thought of as the total dipole moment per unit volume.

Dipole moment,  $M$ , is the product of the charge  $Q$ , and the displacement,  $d$ , between the positive and negative charges [13-16].

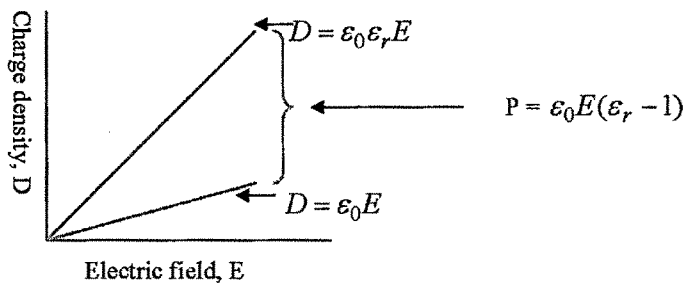


**Fig 2.4 Charge density,  $D$ , versus electric field  $E$ . Polarisation,  $P$ , is that part of the charge density contributed by the material.**

$$M = Qd$$

$$C/m^2 = C.m/m^3$$

There are four categories of polarization, each having different mechanism depending on the type of dipole moment which is established.

Total polarization is the sum of all polarizations.

Total polarization = Integrated sum of all dipole moments per unit volume.

$$P = \frac{1}{V} \sum (M_e + M_i + M_o + M_s) \dots \dots \dots (2.4.4)$$

$M_e$ ,  $M_i$ ,  $M_o$ ,  $M_s$  are dipole moments arises from electronic, atomic, orientation and space charge polarization respectively,  $V$  is the volume.

$$P = P_e + P_i + P_o + P_s \dots \dots \dots (2.4.5)$$

**(ii) Dielectric constant in an alternating field**

When a voltage is applied across the dielectric, energy is stored by one of the following mechanisms. They are

1. Electronic polarization
2. Atomic polarization
3. Orientation polarization
4. Interfacial or Space Charge polarization

Each dielectric mechanism has a characteristic relaxation frequency. As the frequency becomes larger, the slower mechanisms drop off. Electronic polarization occurs in neutral atoms when an electric field displaces the nucleus with respect to the electrons that surround it. Atomic polarization occurs when neighboring positive and negative ions "stretch" under an applied electric field. Both electronic and atomic polarizations create induced moments depending on the polarizability of the atoms or molecules. Unequal sharing of electrons between the atoms of a molecule causes a permanent dipole moment. In the absence of an external electric field, these moments are oriented in a random order such that no net polarization is present. Under an external electric field, the dipoles rotate to align with the electric field causing orientation

polarization to occur. It is this orientation polarization, which is of fundamental importance in dielectric spectroscopy. Interfacial or space charge polarization occurs when the motion of migrating charges is impeded. The accumulated charges distort the field resulting in a net polarization. At high frequencies, electronic and atomic polarizations contribute to energy storage, which involves a resonance phenomenon. At low frequencies, orientation polarization contributes to energy storage and this involves a relaxation phenomenon.

Figure 2.5 illustrates the different mechanisms of polarization of a dielectric material and the effect of frequency on dielectric properties is illustrated in Fig.2.6.

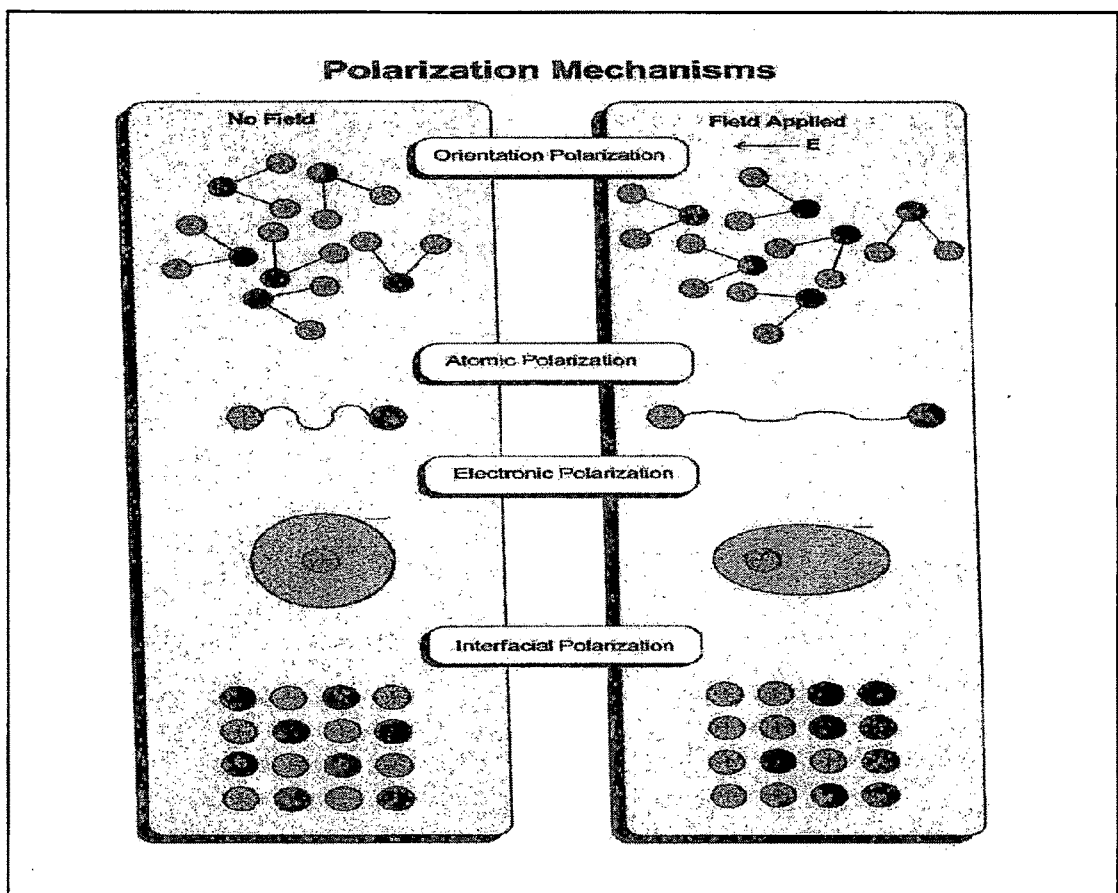


**Fig 2.5 Polarization Mechanisms**

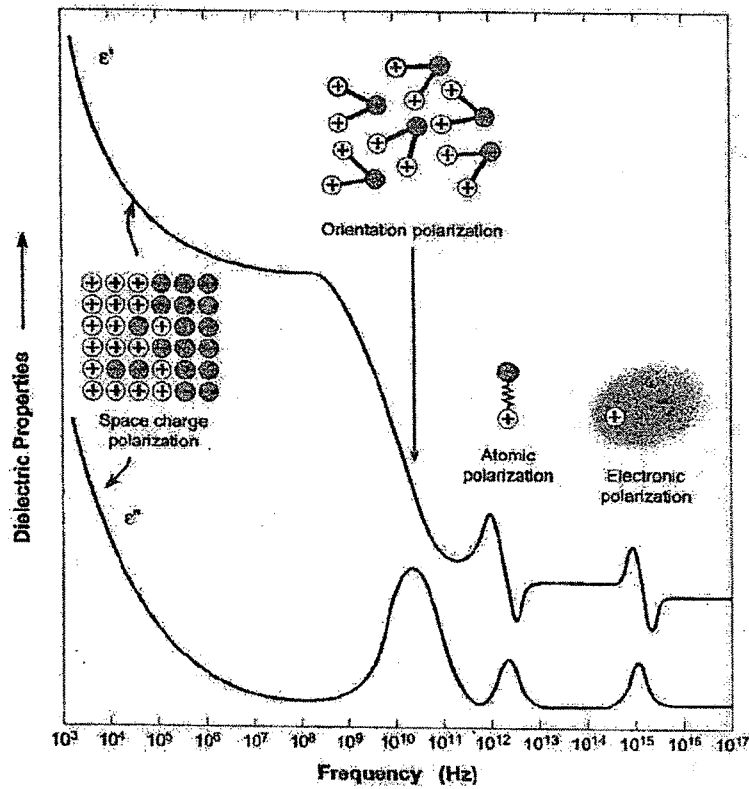


**Fig. 2.6 Effect of frequency on dielectric properties**

The interaction between electromagnetic waves and dielectric material is governed by Maxwell's equation over the entire frequency range. From these equations the relationship between the time varying electric field and magnetic field can be derived. Since both the fields can cause energy storage and energy dissipation in the material, two sets of parameters are required to characterize a dielectric as a carrier of electromagnetic energy. The complex permittivity ( $\epsilon^* = \epsilon' - j\epsilon''$ ) can be considered a fundamental parameter for the macroscopic description of a dielectric, exposed to the alternating field.

A capacitor charged by a sinusoidal voltage source of the angular frequency  $\omega=2\pi f$

$$V = V_0 e^{i\omega t} \dots\dots\dots(2.4.6)$$

stores a charge in vacuum,

$$Q = C_0 V$$

and draws a charging current:

$$I_c = \frac{dQ}{dt} = j \cdot \omega \cdot C_0 \cdot V \dots\dots\dots (2.4.7)$$

where the voltage leads the current by the temporal phase angle of 90°. C<sub>0</sub> is the capacitance of the condenser. If some other substance is used as a dielectric, the condenser increases its capacitance C to

$$C = C_0 \frac{\epsilon'}{\epsilon_0} = C_0 \cdot k' \dots\dots\dots (2.4.8)$$

where ε' and ε<sub>0</sub> are the permittivity of the dielectric medium and vacuum respectively and designates the relative dielectric constant of the dielectric material.

Thus, dielectric constant of dielectric material,

$$K' = \frac{\epsilon'}{\epsilon_0} \dots\dots\dots (2.4.9)$$

Loss tangent is expressed by,

$$\tan \delta = \frac{\epsilon''}{\epsilon'} \dots\dots\dots (2.4.10)$$

where real part ε' defines insulating properties and the imaginary part ε'' describes conductive properties of the dielectric material.

**(iii) Measurement method**

Dielectric properties for the samples were measured by Solartron 1260 Impedance gain phase analyzer. The electrical contact on the sample was made by applying an air drying type of silver paste and than samples was mounted between the two electrode as shown in Fig.2.7.

The continuity was checked and was put in the oven whose temperature could be varied using a variac and was directly read by a thermo voltmeter.



**Fig. 2.7 Impedance gain/phase analyser (Solartron 1260)**

The variation of dielectric properties like Impedance, Capacitance, Dielectric loss and phase with frequency (100 Hz to 10 MHz) and temperature (RT to 80 °C) were noted. These data were used to calculate the real and imaginary part of dielectric constant, real and imaginary part of impedance and the ac conductivity.

The formulae used are as follows:

The general expression for the complex dielectric permittivity ( $\epsilon^*$ ) of a material is considered as

$$\epsilon^* = \epsilon' - i \epsilon'' \dots\dots\dots(2.4 .11)$$

The real part of the permittivity is defined as

$$\epsilon' = Cp/C_0 \dots\dots\dots(2.4.12)$$

Where,  $C_0$  is defined as

$$C_0 = \epsilon_0 A/t$$

Where,  $A$  and  $t$  are the area of electrode and thickness of the sample respectively.  $\epsilon_0$  permittivity of vacuum =  $8.85 \times 10^{-12}$  F/m.

**2.4.2 Conductivity of the composites**

**(i) Theory**

The conductivity of any material is related to its atomic or molecular structure. The electrons of an atom exist in different energy states corresponding to different orbits around the nucleus. Quantum mechanical considerations permit only a certain number of electrons in a given radial orbit. The electrons in a given orbit comprise a shell. If an orbit is filled, additional electrons cannot enter that shell or have an energy associated with that level. The outermost shell contains the valence electrons, whose orbits are usually not filled and are responsible for chemical bonding. As two atoms bond to each other, their interpenetrating electrons may split into valence band and conduction band. These bands are separated by a gap or energy difference. The magnitude of the energy gap determines the conductivity of the material. In highly conductive materials (e.g., metals), the valence band overlaps the conduction band. Therefore, there are numerous energy levels into which an electron can be excited. Under these conditions, the addition of a small external energy raises some of the valence electrons into the conduction band, where they are free to flow. This type of conduction is referred to as band conduction. For less conductive materials, e.g., graphite, the valence band is filled, but the energy gap is so small that it can be easily jumped. Materials conducting by this mechanism are referred to as semiconductors. When the valence band is filled and the energy gap is too large to be easily jumped, the materials are insulators.

In conductor-polymer composites, where a conducting species are added to an insulator, there are three possibilities:

- (a) no contact between particles,
- (b) close proximity,
- (c) physical contact.

When the conducting particles are isolated, the conductivity of the composite is changed only slightly. The composite remains only an insulator, although there may be significant change in its dielectric properties. When the conductive particles are in close proximity, electrons can jump poorly conducting or non-conducting gaps between the particles, although with difficulty, by tunneling or hopping, thus creating current flow [19]. Tunneling is a process by which electrons on one side of the barrier jump to the other side without an energy input. Hopping is similar, but the electron energy must be raised before the barrier can be crossed; that is, the process requires activation energy. The ability of electron to jump a gap, under a given voltage field, increases exponentially with decreasing gap size. Gaps as large as 10 nm can be jumped.

The third condition is possible when conductive particles will physically contact one another to form a continuous network throughout the composite. Under this condition, the composite is expected to conduct through the particles network by the conduction mechanism of the particles. For instance, in such situation, composites using metal particles as the conducting filler should then exhibit band-type conduction.

A capacitor when charged under an a.c. voltage will have some loss in current due to ohmic resistance or impedance by heat absorption. If  $Q$  is the charge in Coulomb due to a potential difference of  $V$  volts between two plates of a condenser of area  $A$ , and interplate distance  $t$ , then a.c. conductivity ( $\sigma_{ac}$ ) due to a.c. voltage  $V$  ( $V_0 e^{j\omega t}$ ) is given by the relation

$$\sigma_{ac} = J/E \dots\dots\dots(2.4.13)$$

Where  $J$  is the current density and  $E$  the electrical field strength vector which is

$$E = D/\epsilon \dots\dots\dots(2.4.14)$$

D being the displacement vector of the dipole charges and is the complex permittivity of the material. For a parallel plate capacitor the electric field intensity (E) is the ratio of the potential difference between the plates of the capacitor to the interplate distance i.e.

$$E = V/t \dots \dots \dots (2.4.15)$$

Since

$Q/A = V\varepsilon/t$ , the current density  $J = dq/dt$  is given by

$$J = \frac{dq}{dt} = \frac{d}{dt} \left( \frac{V\varepsilon}{d} \right) = \frac{\varepsilon}{d} \left( \frac{dV}{dt} \right)$$

$$J = \frac{\varepsilon}{d} Vj\omega \dots \dots \dots (2.4.16)$$

Substituting for E and J in (2.4.13),

$$\sigma_{ac} = J/E = \varepsilon j\omega = (\varepsilon' - j\varepsilon'')j\omega = \varepsilon'j\omega + \omega\varepsilon'' \dots \dots \dots (2.4.17)$$

For the a.c. conductivity to be a real quantity, the term containing j has to be neglected, hence

$$\sigma_{ac} = \omega\varepsilon'' \dots \dots \dots (2.4.18)$$

In any dielectric material, there will be some power loss because of the work done to overcome the frictional damping forces encountered by the dipoles during their rotation. If an a.c. field is considered, then in an ideal case the charging current  $I_c$  will be  $90^\circ$  out of phase with the voltage. But in most of the capacitors due to the absorption of electrical energy some loss current,  $I_L$  will also be produced, which will be in phase with the voltage. Charging current  $I_c$  and loss current  $I_L$ , will make angles  $\delta$  and  $\theta$  respectively with the total current I, passing through the capacitor. The loss current is represented by  $\sin\delta$  of the total current I. Generally  $\sin \delta$  is called the loss

factor but when  $\delta$  is small, the  $\sin\delta = \delta = \tan\delta$ . The two components  $\epsilon'$  and  $\epsilon''$  of the complex dielectric constant  $\epsilon$ , will be frequency dependent,

$$\epsilon' = D_0 \cos\left(\frac{\delta}{E_0}\right) \dots\dots\dots(2.4.19)$$

$$\epsilon'' = D_0 \sin\left(\frac{\delta}{E_0}\right) \dots\dots\dots(2.4.20)$$

Since the displacement vector ( $D_0$ ) in a time varying field will not be in phase with  $E$  and hence there will be a phase difference  $d$  between them. From equation (2.4.19) and (2.4.20), we have

$$\tan\delta = \epsilon''(\omega)/\epsilon'(\omega) \dots\dots\dots(2.4.21)$$

Substituting the value of  $\epsilon''(\omega)$  from (2.4.21) into (2.4.18), we have

$$\sigma_{ac} = \omega\epsilon(\omega) \tan\delta \dots\dots\dots(2.4.22)$$

Where  $\omega = 2\pi f$  and  $\epsilon = \epsilon_0 \epsilon_r$  ( $\epsilon$  is the relative permittivity of the material and  $\epsilon_0$  the permittivity of free space).

So

$$\sigma_{ac} = 2\pi f \epsilon_0 \epsilon_r \tan\delta \dots\dots\dots(2.4.23)$$

Dielectric constant or relative permittivity can be calculated by using the formula

$$\epsilon_r = C \frac{t}{A} \dots\dots\dots(2.4.24)$$

From equations (2.4.23) and (2.4.24) one can get the relation,

$$\sigma = 2\pi f D C \frac{t}{A} \dots\dots\dots(2.4.25)$$

where,  $D$  (Dissipation Factor) =  $\tan\delta$ . The equation (2.4.25) has been used to calculate the a.c. conductivity of the materials at a given frequency.

### 2.4.3 X ray diffraction

X-ray diffraction is a tool for the investigation of fine structure of matter. This technique had its beginnings in von Laue's discovery in 1912 that crystals diffract x-rays, the manner of the diffraction revealing the structure of the crystal. At first, x-ray

diffraction was used only for the determination of crystal structure. Later on, however, other uses were developed, and today the method is applied, not only to structure determination, but to such diverse problems as chemical analysis and stress measurement, to the study of phase equilibria and the measurement of particle size, to the determination of the orientation of one crystal or the ensemble of orientations in a polycrystalline aggregate.

### (i) Principles of X-ray diffraction

X-rays are electromagnetic radiation with a wavelength in the range of  $0.01\text{--}100\text{\AA}$ . X-rays belong to a portion of the electromagnetic spectrum overlapping with gamma rays in the shorter wavelengths and with ultraviolet in the longer wavelengths. The wavelength of typical X-rays used in X-ray diffraction is in the vicinity of  $1\text{\AA}$ , which is comparable to the range of interatomic spacing in crystals. When a monochromatic X-ray beam hits a sample, in addition to absorption and other phenomena, it generates scattered X-rays with the same wavelength as the incident beam. This type of scattering is also known as elastic scattering or coherent scattering.

The scattered X-rays from a sample are not evenly distributed in space, but a function of the electron distribution in the sample. The atomic arrangement in the sample can be ordered like a single crystal or disordered like glass or liquid. As such, the intensities and spatial distributions of the scattered X-rays form a specific diffraction pattern that is uniquely determined by the structure of the sample [20, 21].

### (ii) Bragg Law

There are many theories and equations about the relationship between the diffraction pattern and the material structure. Bragg law is a simple way to describe the diffraction of X-rays by a crystal. In Figure 2.8 (a), the incident X-rays hit the crystal

planes with an incident angle  $\theta$  and reflection angle  $\theta$ . The diffraction peak is observed when the Bragg condition is satisfied

$$n\lambda = 2d \sin\theta \dots\dots\dots(2.4.26)$$

where  $\lambda$  is the wavelength,  $d$  is the distance between each adjacent crystal planes ( $d$ -spacing),  $\theta$  is the Bragg angle at which one observes a diffraction peak, and  $n$  is an integer number, called the order of reflection. That means the Bragg condition with the same  $d$ -spacing and  $2\theta$  angle can be satisfied by various X-ray wavelengths (energies). The first-order reflection ( $n=1$ ) is from the fundamental energy, and the second- or third-order reflections are from harmonic energies, two or three times the fundamental energy.

In X-ray diffraction using a single wavelength, the Bragg equation is typically expressed with  $n=1$  for the first order of diffraction because the higher order reflections can be considered as being from different lattice planes. For instance, the second-order reflection from  $(hkl)$  planes is equivalent to the first-order reflection from  $(2h, 2k, 2l)$  planes. The diffraction peak is displayed as diffracted intensities at a range of  $2\theta$  angles.

For perfect crystals with perfect instrumentation, the peak is a delta function (the dark straight vertical line) as shown in Figure 2.8 (b). The intensity is denoted by  $I$ . The delta function is an oversimplified model that requires a perfect crystal without mosaic structure and a perfectly collimated monochromatic X-ray beam. A typical diffraction peak is a broadened peak displayed by the curved line in Figure 2.8(b).

The peak broadening can be due to many effects, including imperfect crystal conditions, such as strain, mosaic structure, and finite size; ambient conditions, such as atomic thermal vibration and instrumental conditions, such as X-ray beam size, beam divergence, beam spectrum distribution, and detector resolution. The curved

line gives a peak profile, which is the diffracted intensity distribution in the vicinity of the Bragg angle. The highest point on the curve gives the maximum intensity of the peak,  $I_{\max}$ . The width of a peak is typically measured by its full width at half maximum (FWHM). The total diffracted energy of a diffracted beam for a peak can be measured by the area under the curve, which is referred to as integrated intensity. The integrated intensity is a more consistent value for measuring the diffracted intensity of a reflection since it is less affected by all the peak broadening factors. Causes of peak broadening, while increasing FWHM, typically also reduce the maximum intensity at the same time. Therefore, overall variation of the integrated intensity is less significant compared to the variations of FWHM and  $I_{\max}$ .

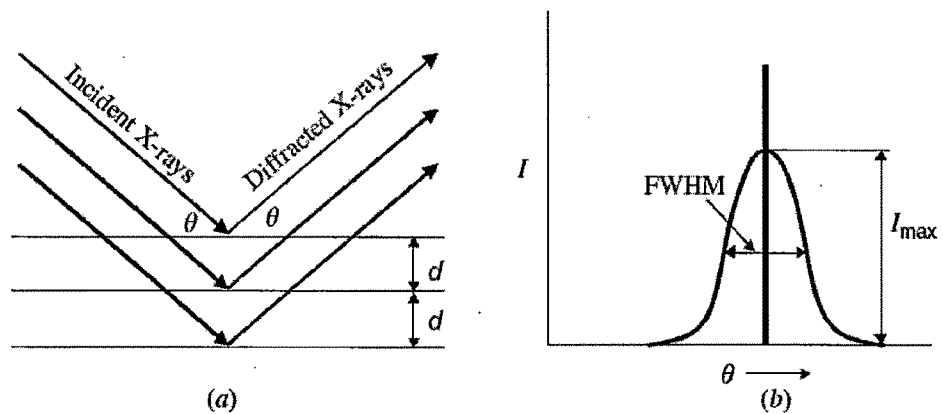


**Fig. 2.8 (a) The incident X-rays and reflected X-rays make an angle of  $\theta$  symmetric to the normal of crystal plane. (b) The diffraction peak is observed at the Bragg angle  $\theta$ .**

### (iii) Instrumentation

X-ray diffraction instruments consist of X-ray generators, goniometers, sample holders, and X-ray detectors such as photographic film or a movable proportional counter. X-ray generators or tubes produce X-rays by bombarding a metal target with high-energy (10 - 100 keV) electrons, which bounces electrons out of the materials

core into its outer shells. As electrons fill holes in the outer shells, the inner shells emit X-ray photons. Two common targets are molybdenum (Mo) and copper (Cu), which have strong  $K_{\alpha}$  X-ray emissions at 0.71073 and 1.5418 Å<sup>0</sup>, respectively. Decelerating electrons in a target or a synchrotron ring also generate X-rays. These sources produce a continuous spectrum of X-rays and require X-ray diffraction instruments with crystal monochromators to select a single wavelength.

**(iv) Determination of crystallite size and crystallinity**

The crystallite size in pristine and irradiated polymer composites was determined by Scherrer formula [22]

$$\text{crystallite size } (L) = \frac{K\lambda}{2d \cos\theta} \dots\dots\dots 2.4.27$$

where K is a constant which varies from 0.89 to 1.39,  $\lambda$  is the wavelength (1.54 Å<sup>0</sup>) for Cu  $K_{\alpha}$ , d is Full width at half maxima (FWHM) and  $\theta$  is the peak position in radian.

The degree of crystallinity of polymer composites is calculated by given formula

$$k = \frac{\text{Area under diffraction peak}}{\text{Total area under diffractogram}} * 100\% \dots\dots\dots (2.4.28)$$

In present work, XRD patterns of pristine as well irradiated polymer composites were recorded on a (model: Shimadzu, XRD-6000/Bruker's X-ray Diffraction-D8) diffractometer with Cu  $K_{\alpha}$  radiation (1.5418 Å) for a Bragg angle 5<sup>0</sup><2 $\theta$ <60<sup>0</sup> at the scanning rate of 1 degree/min. X ray generator operated at a voltage of 40kV and current 30mA.

**2.4.4 Atomic force microscopy (AFM)**

Scanning probe microscopes (SPM) define a broad group of instruments used to image and measure properties of material, chemical, and biological surfaces. SPM images are obtained by scanning a sharp an image. The two primary forms of SPM are scanning tunneling microscopy (STM) and probe across a surface while

monitoring and compiling the tip-sample interactions to provide atomic force microscopy (AFM). STM was first developed in 1982 at IBM, Zurich by Binnig, et al. [23]. The invention of the scanning tunneling microscope (for which Binnig and Rohrer were awarded the Nobel Prize in Physics in 1986) has had a great impact on the technical community by providing a new and unique tool to advance fundamental science and technology. Although the ability of the STM to image and measure material surface morphology with atomic resolution has been well documented, only good electrical conductors are candidates for this technique. This significantly limits the materials that can be studied using STM and led to the development, in 1986, of the atomic force microscope by Binnig, Quate, and Gerber [24]. This enabled the detection of atomic scale features on a wide range of insulating surfaces that include ceramic materials, biological samples, and polymers.

AFM provides a number of advantages over conventional microscopic techniques. AFMs probe the sample and make measurements in three dimensions, x, y, and z (normal to the sample surface), thus enabling the presentation of three-dimensional images of a sample surface. This provides great advantages over any microscope available previously. With good samples (clean, with no excessively large surface features), resolution in the x-y plane ranges from 0.1 to 1.0 nm and in the z direction is 0.01 nm (atomic resolution). AFMs require neither a vacuum environment nor any special sample preparation, and they can be used in either an ambient or liquid environment. With these advantages AFM has significantly impact in the fields of materials science, chemistry, biology, physics, and the specialized field of semiconductors.

Contact mode AFM is one of the more widely used scanning probe modes, and operates by rastering a sharp tip (made either of silicon or  $\text{Si}_3\text{N}_4$  attached to a low

spring constant cantilever) across the sample. An extremely low force ( $\sim 10^{-9}$  N, interatomic force range) is maintained on the cantilever, thereby pushing the tip against the sample as it rasters. Either the repulsive force between the tip and sample or the actual tip deflection is recorded relative to spatial variation and then converted into an analogue image of the sample surface [25]. The principal behind the operation of an AFM in the contact mode is shown in Figure 2.9. The AFM tip is first brought (manually) close to the sample surface, and then the scanner makes a final adjustment in tip-sample distance based on a set point determined by the user. The tip, now in contact with the sample surface through any adsorbed gas layer, is then scanned across the sample under the action of a piezoelectric actuator, either by moving the sample or the tip relative to the other. A laser beam aimed at the back of the cantilever-tip assembly reflects off the cantilever surface to a split photodiode, which detects the small cantilever deflections. A feedback loop, shown schematically in Figure 2.9, maintains constant tip-sample separation by moving the scanner in the z direction to maintain the set point deflection. Without this feedback loop, the tip would “crash” into a sample with even small topographic features (although this phenomenon can happen even with careful AFM operation). By maintaining a constant tip-sample separation and using Hooke’s Law ( $F = -k x$  where  $F$  is force,  $k$  is the spring constant, and  $x$  is the cantilever deflection), the force between the tip and the sample is calculated. Finally, the distance the scanner moves in the z direction is stored in the computer relative to spatial variation in the x-y plane to generate the topographic image of the sample surface.

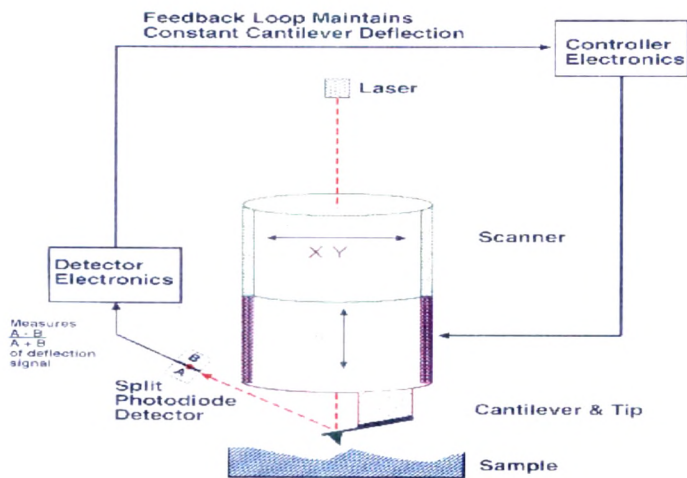


**Fig. 2.9 Schematic diagram showing the operating principles of the AFM in the contact mode.**

Over the years additional modes of operation have been developed for the AFM. The another modes of operation are Tapping Mode and Lift Mode AFM. Although operating in the contact mode has proven successful, it suffers from a number of drawbacks that limit its use on a number of sample types. First, the constant downward force on the tip often damages (and thus changes) many softer surfaces (polymers and biological samples) and even some hard surfaces such as silicon. Also, many samples, such as small particles or biological samples like DNA and cells must be placed on a substrate for imaging purposes. In contact mode, the sample is often destroyed or even pushed out of the field of view by the rastering tip. These complications have been addressed through the development of Tapping Mode AFM. In the Tapping Mode, the AFM tip–cantilever assembly oscillates at the sample surface while the tip is scanned; thus, the tip lightly taps the sample surface while rastering and only touches the sample at the bottom of each oscillation. This prevents damage to soft specimens and avoids the “pushing” of specimens around on the substrate. By using constant oscillation amplitude, a constant tip–sample distance is

maintained until the scan is complete. Tapping Mode AFM can be performed on both wet and dry sample surfaces.

Roughness on pristine and irradiated polymer surfaces is certainly of enormous practical importance for polymer applications. Surface roughening due to irradiation sometimes play an important role in adhesion of functional coatings. However, there is a tendency to neglect the topology at the expense of phase imaging. Generally, tapping mode AFM is less reliable with topology, but it is frequently preferred as phase contrast can be recorded that is usually applied for determining physical and chemical differences in composites [26-27].

For present surface study, Digital Nanoscope IIIa Instrument Inc. is used in tapping mode at IUAC, New Delhi and Nanoscope-E, Digital Instrument from USA in contact mode at UGC-CSR, Indore. Both instruments contain silicon nitride tip attached at the end of cantilever with length of about 100  $\mu\text{m}$  and having 0.5 N/m spring constant. Average surface roughness was determined using this instrument.

#### **2.4.5 Scanning electron microscopy (SEM)**

The scanning electron microscope (SEM) is a type of electron microscope that images the sample surface by scanning it with a high-energy beam of electrons in a raster scan pattern. The electrons interact with the atoms that make up the sample producing signals that contain information about the sample's surface topography, composition and other properties such as electrical conductivity.

A schematic diagram of sample scanning electron microscope is shown in figure.2.10. In SEM, a source of electrons is focused in vacuum into a fine probe that is rastered over the surface of the specimen. The electron beam passes through scan coils and objective lens that deflect horizontally and vertically so that the beam scans the surface of the sample (Figure 2.10). As the electrons penetrate the surface, a number

of interactions occur that can result in the emission of electrons or photons from or through the surface. A reasonable fraction of the electrons emitted can be collected by appropriate detectors, and the output can be used to modulate the brightness of a cathode ray tube (CRT) whose x- and y- inputs are driven in synchronism with the x-y voltages rastering the electron beam. In this way an image is produced on the CRT; every point that the beam strikes on the sample is mapped directly onto a corresponding point on the screen [28]. As a result, the magnification system is simple and linear magnification is calculated by the equation:

$$M = L/l$$

where L is the raster's length of the CRT monitor and l the raster's length on the surface of the sample.

SEM works on a voltage between 2 to 50kV and its beam diameter that scans the specimen is 5nm-2 $\mu$ m. The principle images produced in SEM are of three types: secondary electron images, backscattered electron images and elemental X-ray maps. Secondary and backscattered electrons are conventionally separated according to their energies. When the energy of the emitted electron is less than about 50eV, it is referred as a secondary electron and backscattered electrons are considered to be the electrons that exit the specimen with an energy greater than 50 eV [28]. Detectors of each type of electrons are placed in the microscope in proper positions to collect them.

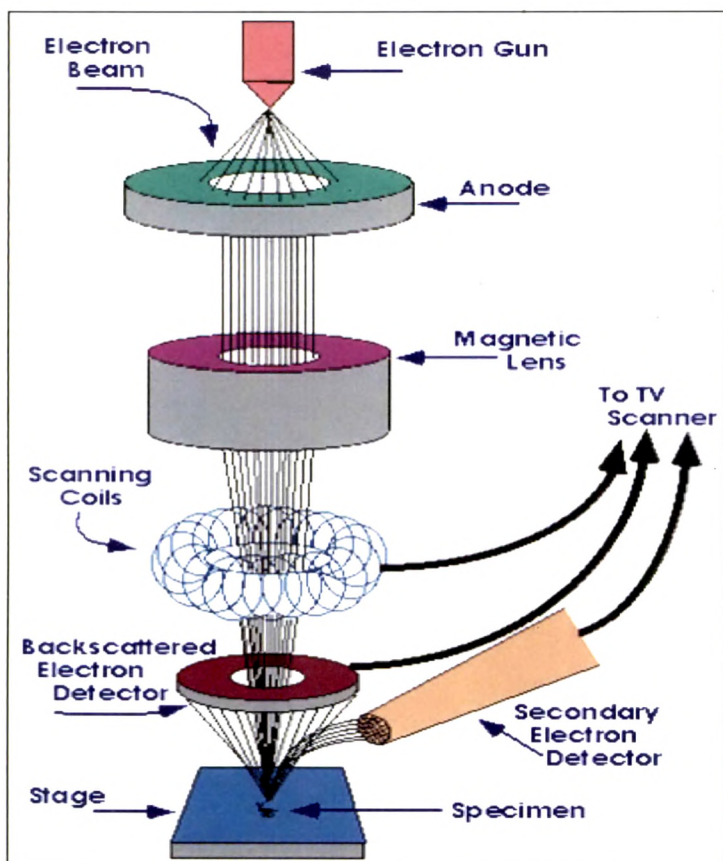


**Fig. 2.10 Geometry of SEM**

Electrons in scanning electron microscopy penetrate into the sample within a small depth, so that it is suitable for surface topology, for every kind of samples (metals, ceramics, glass, dust, hair, teeth, bones, minerals, wood, paper, plastics, polymers, etc). It can also be used for chemical composition of the sample's surface since the brightness of the image formed by backscattered electrons is increasing with the atomic number of the elements. This means that regions of the sample consisting of light elements (low atomic numbers) appear dark on the screen and heavy elements appear bright. Backscattered are used to form diffraction images, called EBSD, that describe the crystallographic structure of the sample. In SEM, X-rays are collected to contribute in Energy Dispersive XRay Analysis (EDX or EDS), which is used to the topography of the chemical composition of the sample.

Consequently, SEM is only used for surface images and both resolution and crystallographic information are limited (because they're only referred to the surface). Other constraints are firstly that the samples must be conductive, so non-conductive materials are carbon-coated and secondly, that materials with atomic number smaller than the carbon are not detected with SEM.

In present work, the SEM images of pristine and irradiated samples were measured by Model: JEOL JSM 5600 instrument (shown in fig.2.11) at Inter University Consortium for Scientific Research (IUC-CSR) Indore.



**Fig. 2.11 SEM/EDAX (JEOL 5600/Oxford INCA) at UGC-CSR Indore**

#### **2.4.6 Differential scanning calorimetry (DSC)**

Thermal analysis refers to a variety of techniques in which a property of a sample is continuously measured as the sample is programmed through a predetermined temperature profile. The most common techniques are thermal gravimetric analysis (TGA) and differential scanning calorimetry (DSC). DSC technique will be discussed here.

##### **(i) Theory**

Differential Scanning Calorimetry is used to determine the enthalpies of a change in the physical state of a material such as melting or transition from one crystalline form to another [29, 30]. DSC is a technique for detecting the temperature difference between the sample and a reference during the process of heating or cooling, which is carried out at a specific rate in identical environments. If a temperature difference develops between the sample and the reference (because of exothermic or endothermic reactions in the sample) the power is adjusted to remove this difference. DSC measures the difference in heat flow between the sample and the reference. A signal proportional to the difference between the heat input to the sample and that to the reference is fed into a recorder. The recorder also registers the average temperature of the sample and the difference, see Figure 2.12.

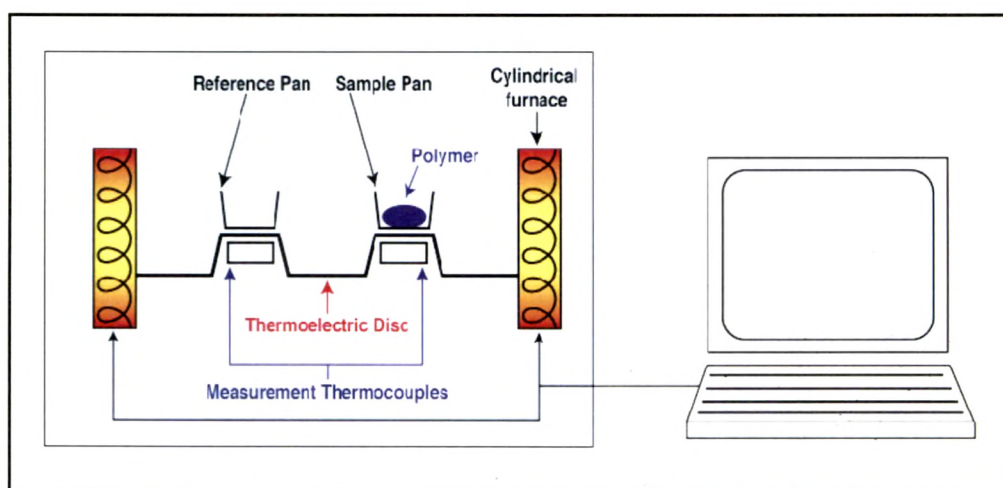


**Fig. 2.12 Schematic representation of the DSC thermal analysis system**

**(ii) Glass transition temperature**

All amorphous polymers exhibit a glass transition temperature. Amorphous regions in partially crystalline polymers exhibit the characteristic changes associated with the polymer at its  $T_g$ . As the polymer is heated, it undergoes a transition. It is characterized by a change in the expansion coefficient and heat capacity. These changes, however, occur over a temperature range. Consequently,  $T_g$  is sometimes

difficult to detect.  $T_g$  is one of the most important parameters that define the properties and behaviour of polymers [31]. Below  $T_g$  the polymer is hard and glassy, while above  $T_g$  it behaves as a rubber and finally as the temperature increases it behaves as a highly viscous liquid (thermoplastic) or degrades (thermosetting). Figure 2.13 illustrates an idealized output (thermogram) from the DSC for  $T_g$  determination. The y-axis is heat flow rate in millicalories/second, and the x-axis is the temperature in °C.  $T_g$  is taken as the midpoint (inflection point) in the thermogram. The  $T_g$  value depends slightly on the rate of flow of heat, being lower for lower rates [32].

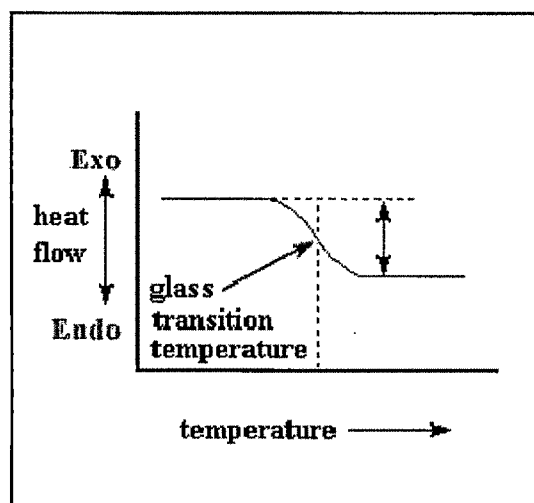


**Fig. 2.13** Ideal DSC output

#### 2.4.7 UV-Visible spectroscopy

The spectroscopy which utilizes the ultraviolet (UV) and visible (VIS) range of electromagnetic radiation, is frequently referred to as Electronic Spectroscopy. The term implies that these relatively high energy photons disturb the electron distribution within the molecule. The ultraviolet region extends from 200-400 nm, whereas visible region lies between 400-800 nm. On passing electromagnetic radiation of ultraviolet and visible regions through a compound, a portion of the radiation is normally absorbed by the compound. The amount of absorption depends on the wavelength of the radiation and structure of the compound. As a result energy

absorption, electrons in the orbital of lower energy state (ground state) are excited to higher energy state (excited state). Since this is electronic excitation phenomena, therefore UV-VIS is sometimes called electronic spectroscopy.

**(i) Beer- Lambert’s Law**

For most spectra the solution obeys Beer’s Law. This states that the light absorbed is proportional to the number of absorbing molecules- *ie.* to the concentration of absorbing molecules. This is only true for dilute solutions. A second law – Lambert’s law – tells us that the fraction of radiation absorbed is independent of the intensity of the radiation. Combining these two laws gives the Beer–Lambert law:

$$\log_{10} \frac{I_0}{I} = \epsilon lc \dots\dots\dots(2.4.29)$$

$I_0$  = the intensity of the incident radiation

$I$  = the intensity of the transmitted radiation

$\epsilon$  = the molar absorption coefficient

$l$  = the path length of the absorbing solution (cm)

$c$  = the concentration of the absorbing species in mol/L

The Beer –Lambert’s law gives the information about the molar absorption coefficient,  $\epsilon$  and  $\lambda_{max}$  which is the wavelength at which maximum absorption occurs. These two pieces of information are sometimes enough to identify a substance.

**(ii) Theory of Electronic transitions**

The absorption of UV or visible radiation corresponds to the excitation of outer electrons. There are three types of electronic transition which can be considered;

1. Transitions involving  $\pi$ ,  $\sigma$ , and  $n$  electrons
2. Transitions involving charge-transfer electrons
3. Transitions involving  $d$  and  $f$  electrons (not covered in this Unit)

When an atom or molecule absorbs energy, electrons are promoted from their ground state to an excited state. In a molecule, the atoms can rotate and vibrate with respect to each other. These vibrations and rotations also have discrete energy levels, which can be considered as being packed on top of each electronic level [33].

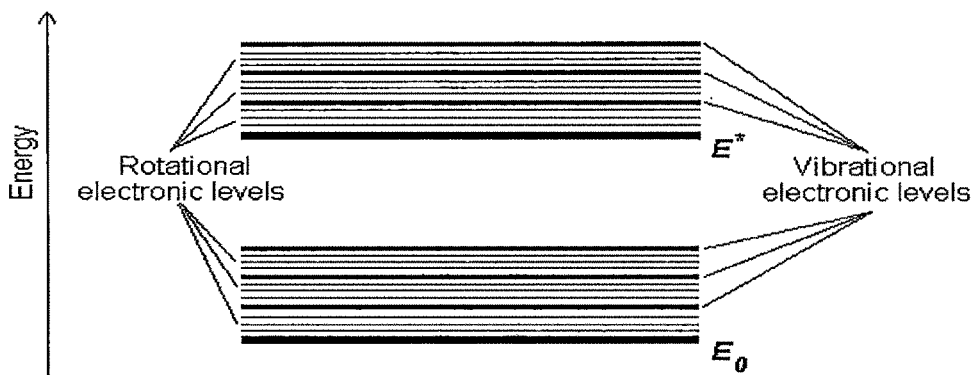


**Fig. 2.14 Absorbing species containing  $\pi$ ,  $\sigma$ , and  $n$  electrons**

Absorption of ultraviolet and visible radiation in organic molecules is restricted to certain functional groups (chromophores) that contain valence electrons of low excitation energy. The spectrum of a molecule containing these chromophores is complex. This is because the superposition of rotational and vibrational transitions on the electronic transitions gives a combination of overlapping lines. This appears as a continuous absorption band.

Possible electronic transitions of  $\pi$ ,  $\sigma$ , and  $n$  electrons are;

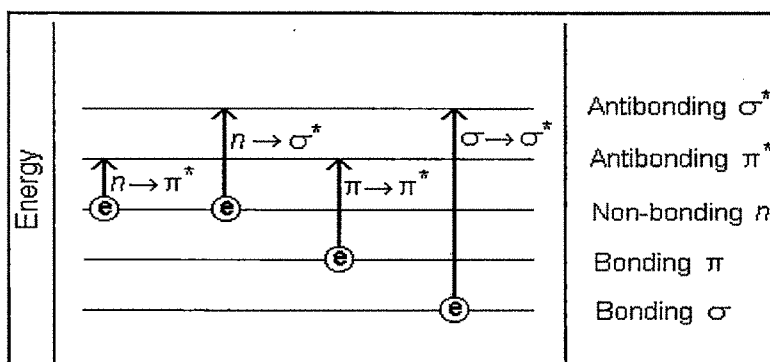


**Fig. 2.15  $\sigma \rightarrow \sigma^*$  Transitions,  $n \rightarrow \sigma^*$  Transitions,  $n \rightarrow \pi^*$  and  $\pi \rightarrow \pi^*$  Transitions**

An electron in a bonding  $\sigma$  orbital is excited to the corresponding antibonding orbital. The energy required is large. For example, methane (which has only C-H bonds, and can only undergo  $\sigma \rightarrow \sigma^*$  transitions) shows an absorbance maximum at 125 nm. Absorption maxima due to  $\sigma \rightarrow \sigma^*$  transitions are not seen in typical UV-Vis. spectra (200 - 700 nm). Saturated compounds containing atoms with lone pairs (non-bonding electrons) are capable of  $n \rightarrow \sigma^*$  transitions. These transitions usually need less energy than  $\sigma \rightarrow \sigma^*$  transitions. They can be initiated by light whose wavelength is in the range of 150 - 250 nm. The number of organic functional groups with  $n \rightarrow \sigma^*$  peaks in the UV region is small.

Most absorption spectroscopy of organic compounds is based on transitions of  $n$  or  $\pi$  electrons to the  $\pi^*$  excited state. This is because the absorption peaks for these transitions fall in an experimentally convenient region of the spectrum (200 - 700 nm). These transitions need an unsaturated group in the molecule to provide the  $\pi$  electrons.

Molar absorptivities from  $n \rightarrow \pi^*$  transitions are relatively low, and range from 10 to 100  $\text{L mol}^{-1} \text{cm}^{-1}$ .  $\pi \rightarrow \pi^*$  transitions normally give molar absorptivities between 1000 and 10,000  $\text{L mol}^{-1} \text{cm}^{-1}$ . The solvent in which the absorbing species is dissolved also has an effect on the spectrum of the species. Peaks resulting from  $n \rightarrow \pi^*$  transitions are shifted to shorter wavelengths (blue shift) with increasing solvent polarity. This arises from increased solvation of the lone pair, which lowers the energy of the  $n$  orbital. Often (but not always), the reverse (i.e. red shift) is seen for  $\pi \rightarrow \pi^*$  transitions. This is caused by attractive polarization forces between the solvent and the absorber, which lower the energy levels of both the excited and unexcited states. This effect is greater for the excited state, and so the energy

difference between the excited and unexcited states is slightly reduced - resulting in a small red shift. This effect also influences  $n \rightarrow \pi^*$  transitions but is over shadowed by the blue shift resulting from solvation of lone pairs.

### (iii) Charge - Transfer Absorption

Many inorganic species show charge-transfer absorption and are called charge-transfer complexes. For a complex to demonstrate charge-transfer behavior one of its components must have electron donating properties and another component must be able to accept electrons. Absorption of radiation then involves the transfer of an electron from the donor to an orbital associated with the acceptor.

### (iv) Instrumentation

An instrument for measuring molecular absorption spectra (UV-VIS) usually consists of a light source, an optical system including a spectral apparatus, a sample compartment, a detector and a system for data acquisition and data processing are shown in Fig.2.16.

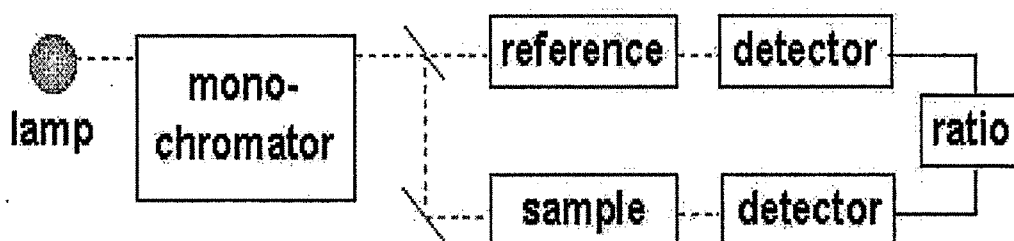


**Fig.2.16 Schematic of a dual beam UV-Vis spectrophotometer**

The light source is usually a deuterium lamp, which emits electromagnetic radiations in the ultraviolet region of the spectrum. A second light source, tungsten lamp, is used for wavelength in the visible region of the spectrum. The monochromator is diffraction grating; its role is to spread the beam of light into its component of wavelengths. A system of slits focuses simultaneously the light of desired wavelength on the sample and reference cell. The spectrometer compares the light passing

through the sample with that passing through the reference cell. Light across the whole range of wavelength is monitored simultaneously. The transmitted light is detected and the spectrometer records and the absorption spectrum by scanning the wavelength of the light passing through the cells. The detector is generally a photomultiplier tube, although in modern instruments photodiodes are used. Both single and double beam instruments are available now. The principle for single beam are the same as for double beam instruments, but data on the reference are taken first, followed by the sample.

**(v) Determinations of band gap**

From the UV-Visible spectra, the indirect and direct optical band gap of all pristine and irradiated composites was determined.

The absorptions (A) of the sample is given by the formula

$$A = 2.303 \log_{10} \frac{I}{I_0} \dots\dots\dots(2.4.30)$$

where I is the intensity of light passing through the samples.

$I_0$  = The intensity of light before passes through the samples.

The absorption coefficient  $\alpha(\nu)$  is obtained by using equation

$$\alpha(\nu) = \frac{A}{d} \dots\dots\dots(2.4.31)$$

Where d is the thickness of the sample in cm

The activation energy  $E_a$  which is the energy corresponding to the absorptions edge  $\lambda_g$  is evaluated by extrapolating the linear portion of  $\alpha(\nu)$  vs.  $h\nu$  curve, to zero absorption value. The activation energy can be determine by the formula

$$E_a = \frac{hc}{\lambda_g} \dots\dots\dots(2.4.32)$$

and the optical band edge can be correlated to the optical band gap  $E_g$  by Tauc expression [34]

$$\omega^2 \varepsilon_2 = (h\omega - E_g)^2 \dots\dots\dots(2.4.33)$$

Where  $\varepsilon_2(\lambda)$  is the optical absorbance,  $\lambda$  is the wavelength and  $\omega = 2\pi\nu$  the angular frequency of the incident radiation.

For the determination of indirect and direct band gap,  $(\alpha h\nu)^{1/2}$  and  $(\alpha h\nu)^2$  were plotted as a function of photon energy ( $h\nu$ ) respectively [35-39] taking into account the linear portion of the fundamental absorption edge of the UV-visible spectra

UV- visible spectra of all pristine and irradiated samples have been studied in wavelength 200-900nm by using U-3000/U-3300 (Hitachi) at IUAC New Delhi.

## References

- [1] A. Qureshi, A. Mergen, S. E. Mehmet, A. Gulluoglu, N.L.Singh, *Macromolecular Science, Part A: Pure Appl. Chem.* 45(2008) 462-469.
- [2] S. Ghosh, R. Mehta, G. K. Chowdhury, A. Rai, P. Patra, B. K. Sahu, A. Pandey, D. S. Mathuria, J. Chacko, A. Chowdhury, S. Kar, S. Babu, M. Kumar, S. S.K. Sonti, K. K. Mistry, J. Zacharias, P. N. Prakash, T. S. Datta, A. Mandal, D. Kanjilal, and A. Roy, *Physical Review special Topics-Accelerators and Beams* 12 (2009) 040101.
- [3] G. Joshi, C. I. Sujo, B. K. Sahu, A. Pandey, B. P. Kumar, J. Karande, in *Proceedings of the Ninth International Conference of Heavy Ion Accelerator Technology, New Delhi, India, 2002* [*Pramana J. Phys.* 59(2002) 1035].
- [4] D Kanjilal, S Chopra, M M Narayanan, I S Iyer, V Jha, R Joshi and S K Datta, *Nucl. Instrum. Methods A* 328 (1993) 97.
- [5] P N Prakash et al, *Proc. Asian Particle Accelerator Conference APAC01*, 17–21 September 2001, Beijing, China, p. 115
- [6] NSC School on Accelerator Physics, NSC, 1989
- [7] R.G.Herb, *Nucl. Instr. Meth. B* 122(1974) 97.
- [8] J. F. Ziegler, J. P. Biersack, and U. Littmark, *The Stopping and Range of ions in solids. Vol. 1* Pergamon Press, New York. 2000.
- [9] J. F. Ziegler, *SRIM-2003 Nucl. Instrum. Meth. B* 219 (2004) 1027-36
- [10] J.C.Maxwell, *A.Treastise on Electricity and Magnetism* (Clarendon Press, Oxford 1881).
- [11] P.Debye, "Some results of Kinetic theory of isolaters" *Physikalische Zeiteschrift* 13(1912)97.
- [12] L. A. Dissado and R.M. Hill., *Nature*, 279 (1979) 685-689.

- [13] L.A. Dissado and R.M. Hill, Proceedings of the Royal Society .London .A, 390(1983) 131-180.
- [14] L.A. Dissado and R.M. Hill, J. chemical Society, Faraday Transactions. 2, Vol 80 (1984) 291-319.
- [15] L.A. Dissado and R.M. Hill., J. Physics :Condense Matter 3(1991) 9773-9790.
- [16] Dissado L.A and Hill R.M, Solid State Ionics 26(1988) 295-297.
- [17] L.A. Dissado and R.M. Hill., The American Physical Society, Physical Review B, 37( 7) (1988) 3434-3439.
- [18] A.K Jonscher, "Dielectric relaxation in solids", Chelsea Dielectric Press 1983, ISBN:0950871109.
- [19] D. Toker, D. Azulay, N. Shimoni, I. Balberg, and O. Millo, Tunneling and percolation in metal-insulator composite materials, Phy. Rev. B **68** (2003) 041403(R)
- [20] B. D.Cullity. Element of X ray diffraction.Addision- Wesley Publishing company.
- [21] Bob B.He. Two dimensional x-ray diffraction . Wiley a John Wiley & Sons, Inc., Publication.
- [22] Scherrer P. Gott Nachar 2 (1918) 98.
- [23] G. Binning and C.F. Quate, Atomic Force Microscopy. Phy. Rev. Lett. 56 (1986) 930.
- [24] G. Binnig, H. Rohrer, Ch. Gerber, and E. Weibel, Surface Studies by Scanning Tunneling Microscopy. Phys. Rev. Lett. 49 (1982) 57-61.
- [25] Cheryl R. Blanchard, Atomic Force Microscopy The Chemical Educator, Publisher: Springer Berlin / Heidelberg ISSN1430-4171 Issue Volume 1, Number 5 / December, 1996.

- [26] A. Karbach, D. Drechsler: Atomic force microscopy – a powerful tool for industrial applications. *Surface and Interface analysis* 27 (1999) 401-409.
- [27] G. Kaupp “Atomic Force Microscopy, Scanning Nearfield Optical Microscopy and Nanoscratching” Springer, Berlin, Heidelberg, New York, 2006.
- [28] R.F. Egerton. *Electron Energy-Loss Spectroscopy in the Electron Microscope*.
- [29] C. Richard Brundle, Charles A. Evans Jr, Shaun Wilson. *Encyclopedia of materials characterization*, Butterworth-Heinemann publications, 1992.
- [30] B. Stuart, “Polymer Analysis”, John Wiley & Sons, Chichester, 2002.
- [31] *Hand book of thermal analysis and calorimetry* , volume 1 editor Michael E Brown.
- [32] V.A. Bershtien, “Differential Scanning Calorimetry of Polymers”, Ellis Horwood, Chichester, 1994.
- [33] J.C Anderson, K.D Leaver, R.D Rawlings, J.M. Alexander, *Material Science*, Third Edition, Chapman and Hall, ISBN 0442306261, 1985
- [34] J. Tauc, R. Grigorovici and A. Vancu, *Phys. Stat. Sol.* 15 (1966) 627.
- [35] [http://www.cem.msu.edu/~reusch/VirtualText/Spectrpy/UV Vis/spectrum.htm](http://www.cem.msu.edu/~reusch/VirtualText/Spectrpy/UV%20Vis/spectrum.htm)
- [36] A. V. Kokate, U. B. Suryavanshi and C. H. Bhosale, *Solar Energy* 80 (2006) 156.
- [37] A. I. Mukolu, *Indian J.Pure App.Phys.*43 (2005) 359.
- [38] M.A.Osman, A. Othman and M. A .Abd-Alla, *J. Phys. D : Appl. Phys.* 24 (1991) 1203.
- [39] J. G. Sole, L. E. Bausa L E and Jaque D, *Introduction to optical spectroscopy of inorganic solids*, John Wiley, New York, 2005.